Measurement of the motional sidebands of a nanogram-scale oscillator in the quantum regime

M. Underwood, D. Mason, D. Lee, H. Xu, L. Jiang, A. B. Shkarin, K. Børkje, S. M. Girvin, and J. G. E. Harris

Phys. Rev. A **92**, 061801 — Published 2 December 2015

DOI: 10.1103/PhysRevA.92.061801

Measurement of the motional sidebands of a nanogram-scale oscillator in the quantum regime

M. Underwood,[1] D. Mason,[1] D. Lee,[1,2] H. Xu,[1] L. Jiang,[1] A. B. Shkarin,[1]
K. Børkje,[1,3] S. M. Girvin,[1,4] and J. G. E. Harris[1,4]

[1] Department of Physics, Yale University, New Haven, CT, 06511, USA
[2] Department of Physics, University of California, Santa Barbara, CA, 93106, USA
[3] Royal Norwegian Naval Academy, Bergen, Norway
[4] Department of Applied Physics, Yale University, New Haven, CT, 06511, USA

We describe measurements of the motional sidebands produced by a mechanical oscillator (with effective mass 43 ng and resonant frequency 705 kHz) that is placed in an optical cavity and cooled close to its quantum ground state. The red and blue sidebands (corresponding to Stokes and anti-Stokes scattering) from a single laser beam are recorded simultaneously via a heterodyne measurement. The oscillator's mean phonon number $\bar{n}$ is inferred from the ratio of the sidebands, and reaches a minimum value of 0.84 ± 0.22 (corresponding to a mode temperature $T = 28 \pm 7\ \mu\mathrm{K}$). We also infer $\bar{n}$ from the calibrated area of each of the two sidebands, and from the oscillator's total damping. The values of $\bar{n}$ inferred from these four methods are in close agreement. The behavior of the sidebands as a function of the oscillator's temperature agrees well with theory that includes the quantum fluctuations of both the cavity field and the mechanical oscillator.

Cavity optomechanical systems operating in the quantum regime are expected to play an important role in advancing the control of electromagnetic fields and mechanical oscillators, interfacing disparate quantum systems, detecting gravitational waves, constraining modifications to orthodox quantum mechanics, and testing hypotheses about quantum gravity.[1,2,3,4,5,6,7,8,9,10,11] The utility of optomechanical systems in these areas reflects their particular combination of long relaxation times, unitary coupling to electromagnetic fields in the microwave and near-infrared domains, and access to the quantum behavior of massive objects.

Optomechanical experiments have been based primarily on systems in which the mechanical oscillator and the cavity field are prepared in Gaussian states, couple weakly to each other at the quantum level (i.e., the bare optomechanical coupling rate g_0 is much less than the oscillator frequency ω_m and the cavity damping rate κ), and are probed via linear measurements of the fields leaving the cavity. (Some optomechanics experiments have demonstrated nonlinear measurements of the cavity fields,[12,13] although without resolving non-Gaussian behavior.) Within this paradigm of Gaussian states, weak coupling, and linear measurements, quantum effects can manifest themselves as apparent fluctuations of quantities which, according to classical mechanics, could be noiseless.[14] Depending on the specific type of measurement, these quantum fluctuations may be ascribed to the cavity field, the mechanical oscillator, or both.[15,16]

One such experiment is a heterodyne measurement of the light leaving an optomechanical cavity that is driven on resonance by a single laser. Classically, the thermal motion of the mechanical oscillator inside the cavity adds modulation sidebands to the laser beam. In the spectrum of the heterodyne signal, the area of these sidebands will be equal, and will be proportional to the oscillator's temperature.

In the quantum treatment described in Refs.[15,16] of the same measurement, the heterodyne spectrum arises from four distinct components: (*i*) the quantum fluctuations of the electromagnetic field, which results in a noise floor equivalent to shot noise; (*ii*) the oscillator's thermal motion, which produces sidebands each with area proportional to the oscillator's mean phonon number $\bar{n}$ (as in the classical case described above); (*iii*) the oscillator's zero point motion, which makes an additional contribution to each sideband that is equivalent to increasing $\bar{n}$ by ½; and (*iv*) the oscillator's response to the quantum fluctuations of the cavity field, which makes a contribution to the Stokes (red) sideband that is equivalent to increasing $\bar{n}$ by ½ and a contribution to the anti-Stokes (blue) sideband that is equivalent to decreasing $\bar{n}$ by ½. The sign difference between the two contributions from (*iv*) reflects the correlations between the quantum fluctuations of the electromagnetic field and the oscillator's motion.

These components are illustrated schematically in Fig. 1(a). Although a measurement of the heterodyne signal only reveals the sum of these contributions, a complete explanation of the full spectrum (particularly as a function of the oscillator's temperature) requires all four components. In addition, some models of quantum gravity predict that the quantum sideband contributions (*iii*) and (*iv*) will occur at slightly different frequency than the thermal sideband contribution (*ii*), in which case they could in principle be resolved separately.[6]

A handful of experiments have measured both optomechanical sidebands in the quantum regime.[17,18,16,19,13] Here we describe an experiment which extends these measurements to a mechanical oscillator with substantially greater effective mass m and lower frequency ω_m than in previous work. Increased m and decreased ω_m are important for realizing, e.g., the proposals in Refs.[5,6]. More broadly, the particular type of oscillator used here (a Si_3N_4 membrane) has been shown to be well-suited to a range of applications in quantum optomechanics.[8,9,20,21,22,23,24,25,26,27,28]

In the experiments described here, both sidebands are produced by a single laser and are measured simultaneously. This is in contrast with most earlier experiments, in which the sidebands were produced using two separate drives applied at once[16,19] or at different times.[17,13] We find that the behavior of the sidebands and other aspects of the data agree well with theory over a wide range of oscillator temperatures, extending to $\bar{n} < 1$.

The experimental setup is shown in Fig. 1(b). The mechanical oscillator is a Si_3N_4 membrane with dimensions 1 mm × 1 mm × 50 nm.[29] The mechanical mode of interest is the membrane's (2,2) vibrational mode.[30] This mode has effective mass m = 43 ng, resonant frequency $\omega_m/2\pi$ = 705.2 kHz, and mechanical linewidth $\gamma_m/2\pi$ that varies between 0.07 – 0.14 Hz. The membrane is positioned inside a free-space Fabry-Pérot cavity with linewidth $\kappa/2\pi$ = 165 kHz (finesse = 40,000). The cavity is single-sided, with κ_{in}/κ = 0.4. All measurements are performed in reflection. The membrane and optical cavity are mounted in a ^{3}He cryostat. Details of the cryogenic setup are given in Ref. [25].

Two lasers are used for these experiments: one for measurements and one for cooling (ML and CL in Fig. 1(b)). Both are Nd:YAG lasers with wavelength λ = 1,064 nm. The lasers address cavity modes whose longitudinal mode numbers differ by two. To accomplish this, the CL is frequency-locked to the ML with an offset approximately equal to twice the cavity's free spectral range ($2 \times \omega_{FSR}/2\pi \approx 8$ GHz). The precise value of this offset is chosen so that the CL is detuned from its cavity mode by an amount $\Delta_{CL} \approx -\omega_m$ to provide optimal laser cooling.

Each laser passes through a filter cavity (FC1 and FC2 in Fig. 1(b)) with linewidth ~20 kHz, reducing classical noise power at ω_m by ~4,000. We do not observe any signature of classical laser noise in the measurements described here, consistent with independent characterization of the filtered beams.

The ML is split into two beams: a probe and a local oscillator (LO). An acousto-optic modulator (AOM) shifts the probe by $\omega_{LO}/2\pi$ = 80 MHz and an electro-optic modulator (EOM) allows for Pound-Drever-Hall (PDH) locking to the cryogenic cavity. The probe beam, LO beam, and cooling beam pass through a fiber-coupled AOM that is driven by a voltage controlled oscillator (VCO). The VCO frequency is tuned by the PDH error signal, so that all the beams track fluctuations in the cryogenic cavity. The beams and the cavity modes are illustrated in Fig. 1(c). The power in the probe and LO beam incident on the cavity were P_{probe} = 32 μW and P_{LO} = 1.57 mW.

As shown in Fig. 1(c), the probe beam drives the cavity nearly on resonance and acquires sidebands from the membrane's motion. Light from the cavity then falls on a photodiode, where the LO and motional sidebands mix to produce photocurrent signals at $\omega_{LO} \pm \omega_m$. Two demodulators are used to simultaneously monitor the photocurrent at frequencies near $\omega_{LO} \pm \omega_m$. The power spectral density (PSD) of these two records are $S_{II}^{(r)}(\omega)$ and $S_{II}^{(b)}(\omega)$ (corresponding to the vicinity of the red and blue sidebands), where ω is the frequency separation from the heterodyne carrier.

The noise floors of $S_{II}^{(r)}$ and $S_{II}^{(b)}$ were found to increase linearly with the total power at the photodiode, as expected for shot noise. The slope of this relationship was used to determine the overall gain G of the detector. G was found to differ by 0.5% between $\omega = \pm\omega_\mathrm{m}$. The overall detection efficiency η was determined by measuring the photodiode's detection efficiency and the loss in the beam path. The detector dark noise was found to differ by 1.5% between $\omega = \pm\omega_\mathrm{m}$. The mechanical sidebands' central frequency ($\tilde{\omega}$) and linewidth ($\tilde{\gamma}$) differ from the membrane's intrinsic values (ω_m and γ_m) because of the optical spring and damping effects.[1] Measuring $\tilde{\omega}$ and $\tilde{\gamma}$ as a function of P_CL (the cooling laser power) and fitting to the expected form gives $g_0/2\pi = 2.2$ Hz. The detuning of the probe beam $\Delta_\mathrm{probe}/2\pi = -6.5$ kHz was determined from $\tilde{\omega}$ and $\tilde{\gamma}$ when $P_\mathrm{CL} = 0$ W. These values of G, g_0, η, and Δ_probe were used to convert $S_{II}^{(\mathrm{r})}$ and $S_{II}^{(\mathrm{b})}$ into the PSD of the inferred membrane displacement $S_{xx}^{(\mathrm{r})}$ and $S_{xx}^{(\mathrm{b})}$, as described in Ref.[31].

Typical records of $S_{xx}^{(\mathrm{r})}$ and $S_{xx}^{(\mathrm{b})}$ are shown in Fig. 2 for different values of P_CL. Qualitatively, these show the expected features described above: a noise floor corresponding to the detector's dark noise plus the shot noise, and motional sidebands at $\pm\omega_\mathrm{m}$. As P_CL increases, the motional sidebands become smaller and broader (owing to optical cooling). At the higher values of P_CL, the blue sideband is distinctly smaller than the red sideband.

In addition to these expected features, peaks are also visible at $\omega/2\pi = \pm 699$ kHz and ± 701 kHz. These peaks appear symmetrically about ω_LO and are not observed when $\Delta_\mathrm{probe} >> \kappa$, indicating that they are due to motion in the cavity. The frequency, linewidth, and area of these peaks are independent of P_CL and Δ_CL, indicating that they are associated with relatively stiff mechanical modes. Together, these observations suggests that these peaks are due to thermal motion of the cavity spacer and/or mirrors.

For each value of P_CL the measured $S_{xx}^{(\mathrm{r})}$ and $S_{xx}^{(\mathrm{b})}$ were fit to the expression[31]

$$S_{xx}^{(\mathrm{r,b})}(\omega) = b^{(\mathrm{r,b})} + s^{(\mathrm{r,b})}(\tilde{\gamma}/2)^2[(|\omega| - \tilde{\omega})^2 + (\tilde{\gamma}/2)^2]^{-1} \qquad (1)$$

These fits are the black curves in Fig. 2. Six fitting parameters are used: $\tilde{\omega}$, $\tilde{\gamma}$, $b^{(\mathrm{r})}$ and $b^{(\mathrm{b})}$ (the noise floors of the red and blue sidebands), and $s^{(\mathrm{r})}$ and $s^{(\mathrm{b})}$ (the amplitudes of the red and blue sidebands). As described above, $b^{(\mathrm{r})}$ and $b^{(\mathrm{b})}$ scale linearly with P_CL, and are consistent with a gain difference 0.5% between the red and blue sidebands.

Figure 3 shows a summary of the fits. Figure 3(b) shows $\tilde{\gamma}/2\pi$, which increases with P_CL and reaches a maximum value 4.86 ± 0.62 kHz. Figure 3(c) shows the inverse of the sidebands' areas $1/A^{(\mathrm{r})}$ and $1/A^{(\mathrm{b})}$ (where $A^{(\mathrm{r,b})} \equiv \frac{1}{4}\tilde{\gamma}s^{(\mathrm{r,b})}$). Both increase with P_CL, but at higher values of P_CL, $1/A^{(\mathrm{r})}$ saturates while $1/A^{(\mathrm{b})}$ continues to increase. Figure 3(d) shows a measure of the sideband asymmetry, $\xi \equiv (A^{(\mathrm{r})}/A^{(\mathrm{b})} - 1)$. ξ increases with P_CL, reaching a maximum value of 1.18 ± 0.32. Errors quoted in the text and error bars in the figures correspond to one standard deviation of statistical uncertainty in the fits to Eq. (1).

The membrane's mean phonon number $\bar{n}$ can be inferred from these measurements in a number of ways. Below, we use four different methods, each of which is directly connected to one of the quantities ξ, $A^{(r)}$, $A^{(b)}$, and $\tilde{\gamma}$.

Sideband asymmetry: As summarized above, the ratio of the sideband areas gives a direct estimate of the mean phonon number:[15,16] $\bar{n} = 1/\xi$. This method is independent of the calibration of the heterodyne signal and does not require knowledge of γ_m or the bath temperature T_{bath}. It does require knowledge of Δ_{probe} (since a detuned probe beam results in unequal filtering of the sidebands by the cavity[31]) and assumes that the lasers' classical noise can be neglected. The values of $\bar{n}$ resulting from this method are the green points in Fig. 3(e). The lowest value is $\bar{n} = 0.84 \pm 0.22$.

Calibrated displacement: Each of the displacement spectra $S_{xx}^{(r)}$ and $S_{xx}^{(b)}$ can be used to estimate $\bar{n}$ via the equipartition theorem.[31] For the blue sideband $\bar{n} = A^{(b)}/2x_{ZP}^2$, while for the red sideband $\bar{n} + 1 = A^{(r)}/2x_{ZP}^2$, where $x_{ZP} = (\hbar/2m\omega_m)^{1/2}$. These estimates do not require knowledge of γ_m or T_{bath}, but do depend upon the calibration of the heterodyne signal. The values of $\bar{n}$ resulting from this method are the red and blue points in Fig. 3(e). The lowest value is $\bar{n} = 0.88 \pm 0.27$ (from the red sideband) and $\bar{n} = 0.86 \pm 0.16$ (from the blue sideband).

Total damping rate: When the probe beam and cooling beam address different cavity modes, $\tilde{\gamma}$ can be used to estimate $\bar{n}$ via[32,33,31]

$$\bar{n} = (\bar{n}_{bath}\gamma_m + \bar{n}_{CL}\gamma_{CL} + \bar{n}_{probe}\gamma_{probe})/\tilde{\gamma} \qquad (2)$$

Here $\bar{n}_{CL,probe} = -\left(\left(\omega_m + \Delta_{CL,probe}\right)^2 + \left(\frac{\kappa}{2}\right)^2\right)/4\omega_m\Delta_{CL,probe}$ each represent the mean phonon number of an oscillator in equilibrium with the quantum fluctuations of a driven cavity mode, and $\bar{n}_{bath} = k_B T_{bath}/\hbar\tilde{\omega}$.

This method is independent of the heterodyne calibration, but requires knowledge of γ_m and T_{bath}. Mechanical ringdown measurements result in a value of $\gamma_m/2\pi$ between 0.07 – 0.14 Hz; here we use $\gamma_m/2\pi = 0.14$ Hz. To estimate T_{bath}, two RuO_2 thermometers were monitored during the experiment: one attached to the ^3He pot, and the other attached to the stage with the membrane chip. Since neither thermometer was in direct contact with the membrane chip, we assume that T_{bath} is a weighted average of these two readings: $T_{bath} = \alpha T_{stage} + (1 - \alpha)T_{pot}$. We choose α to be the value for which the $\bar{n}(P_{CL})$ determined from Eq. (2) have the least squared difference from the $\bar{n}(P_{CL})$ determined from the sideband asymmetry (green points in Fig. 3(e)). This fitting procedure gives $\alpha = 0.498$. The corresponding T_{bath} is shown as the solid points in Fig. 3(a). The values of $\bar{n}$ resulting from this method are the yellow points in Fig. 3(e). The lowest value is $\bar{n} = 0.88 \pm 0.10$.

The solid lines in Figs. 3(b)-(e) are the predicted values of $\tilde{\gamma}$, $1/A^{(\mathrm{r})}$, $1/A^{(\mathrm{b})}$, ξ, and $\bar{n}$. In each case they are calculated from the measured values of the parameters Δ_{CL}, Δ_{probe}, P_{CL}, P_{probe}, P_{LO}, γ_{m}, κ, κ_{in}, T_{bath}, g_0, m_{eff}, ω_{m}, η, and G using the expressions in Ref.[31].

The four estimates of $\bar{n}$ shown in Fig. 3(e) are based on different physical principles, and on different aspects of the data. Their systematic and statistical uncertainties are not completely independent, but their agreement over a wide range of temperature indicates that the system is accurately described by the standard theory of optomechanical systems in the quantum regime.

In the course of this work we became aware of parallel studies.[34]

We acknowledge support from AFOSR (FA9550-90-1-0484 and FA9550-15-1-0270) and NSF (DMR-1301798 and PHY-0855455). K. B. acknowledges financial support from The Research Council of Norway and from the Danish Council for Independent Research under the Sapere Aude program. We thank Yanbei Chen, Aashish Clerk, Huub Janssen, Florian Marquardt, and Yeubin Ning for assistance.

Figure Captions

Fig. 1 (color online): Schematic of the measurements. (a) Contributions to the heterodyne measurement described in the text. Contributions from the shot noise (green), the oscillator's zero point motion (red), and the oscillator's response to the quantum fluctuations of the cavity field (blue) are shown in the vicinity of the red sideband (left) and the blue sideband (right). The total signal is the black curve. (b) The experimental setup. Free space beams, optical fibers, and electrical circuits are colored lines, hollow lines, and thick black lines, respectively. Beams from two lasers (ML, CL) pass through filter cavities (FC1, FC2). The probe beam is shifted by AOM1, while AOM2 tracks fluctuations in the cryogenic cavity. Light is delivered to (and collected from) the cryostat by a circulator. Control circuits, photodiodes, and fiber couplers are indicated by triangles, semicircles, and ovals, respectively. The mechanical oscillator is shown in purple. (c) The spectrum of the lasers (orange, light green, and dark green), cavity modes (black), and mechanical sidebands (red and blue).

Fig. 2 (color online): Motional sidebands of the mechanical oscillator. The membrane's displacement power spectral density S_{xx} is plotted versus the measurement frequency ω. The red data (left panels) show the red sideband $S_{xx}^{(\mathrm{r})}$, and the blue data (right panels) show the blue sideband $S_{xx}^{(\mathrm{b})}$. From top to bottom, the cooling laser power is $P_{\mathrm{CL}} = 0, 34, 158, 415$ μW. The black line is the fit described in the text. The red/blue shading indicates the Lorentzian portion of the fit, specified by $\tilde{\omega}$, $\tilde{\gamma}$, $s^{(\mathrm{r})}$, and $s^{(\mathrm{b})}$. The gray shading indicates the fitted noise floor (shot noise plus dark noise), specified by $b^{(\mathrm{r})}$ and $b^{(\mathrm{b})}$. The detuning of the probe beam causes the displacement imprecision to differ slightly between the red and blue data; as a visual guide, the vertical axes are shifted to compensate for this difference. The data was fit over the range $702\ \mathrm{kHz} \leq |\omega/2\pi| \leq 714\ \mathrm{kHz}$. As P_{CL} increases, laser cooling causes the sidebands to broaden and shrink. In the lowest panel, the ratio of their areas is $\xi + 1 = 2.18 \pm 0.32$, corresponding to $\bar{n} = 0.84 \pm 0.22$.

Fig. 3 (color online): Behavior as a function of cooling laser power P_{CL}. (a) Temperature recorded by two thermometers (T_{pot} and T_{stage}, hollow points) and the membrane's inferred bath temperature T_{bath} (solid points). Note $T_{\mathrm{pot}} < T_{\mathrm{stage}}$. (b) Mechanical linewidth $\tilde{\gamma}/2\pi$. (c) Inverse area of each sideband, $1/A^{(\mathrm{r})}$ and $1/A^{(\mathrm{b})}$. (d) Sideband asymmetry ξ. (e) Inverse mean phonon number $1/\bar{n}$, determined from ξ (green), $A^{(\mathrm{r})}$ (red), $A^{(\mathrm{b})}$ (blue), and $\tilde{\gamma}$ (yellow). Solid lines in (b) – (e) are calculated values, as described in the text. Each inset shows a detailed view of the data for low P_{CL}.

Figure 1

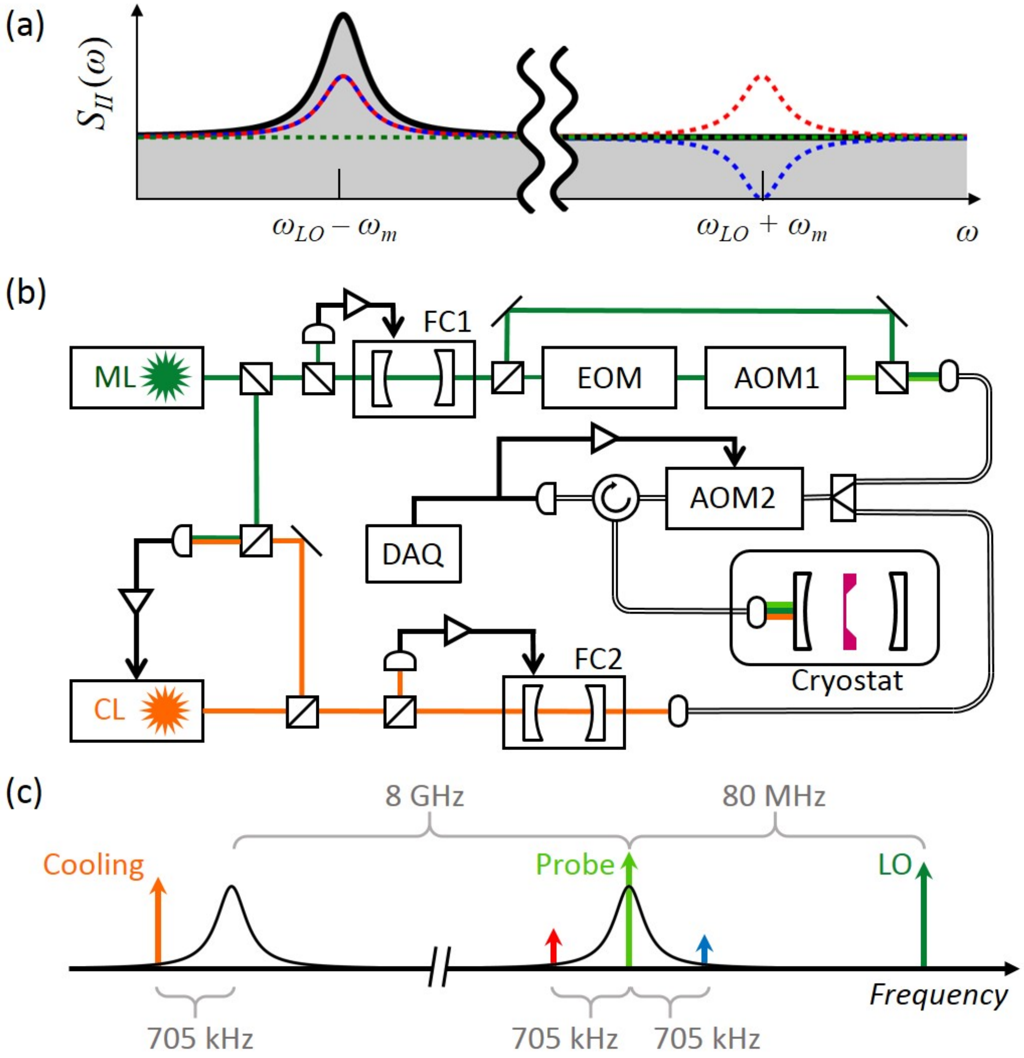

(a)
S_II(ω)
ω_LO − ω_m
ω_LO + ω_m
ω
(b)
FC1
ML
EOM
AOM1
AOM2
DAQ
Cryostat
CL
FC2
(c)
8 GHz
80 MHz
Cooling
Probe
LO
705 kHz
705 kHz
705 kHz
Frequency

Figure 2

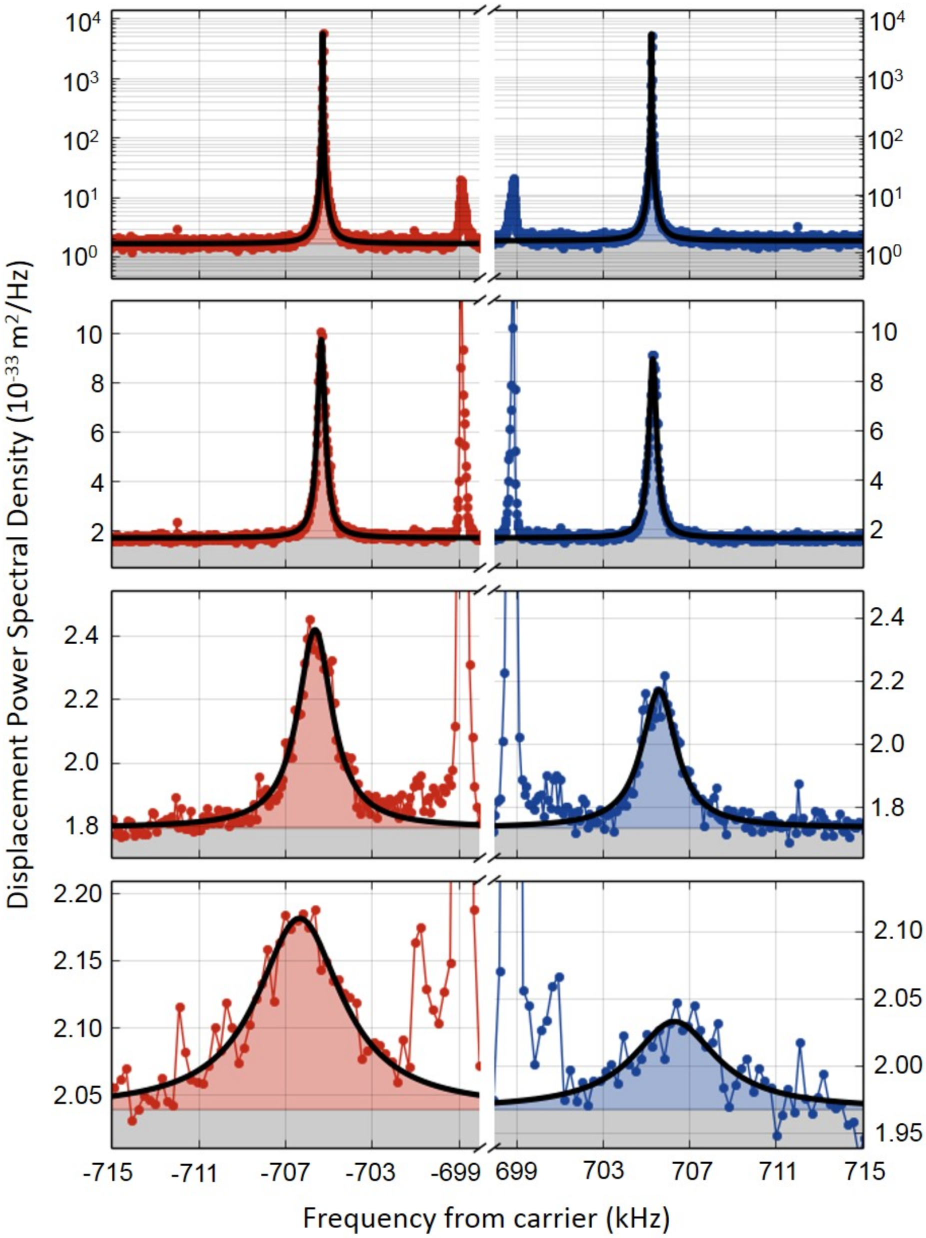

Displacement Power Spectral Density (10^{-33} m^2/Hz)
10^4
10^3
10^2
10^1
10^0
10
8
6
4
2
2.4
2.2
2.0
1.8
2.20
2.15
2.10
2.05
1.95
2.00
-715
-711
-707
-703
-699
699
703
707
711
715
Frequency from carrier (kHz)

Figure 3

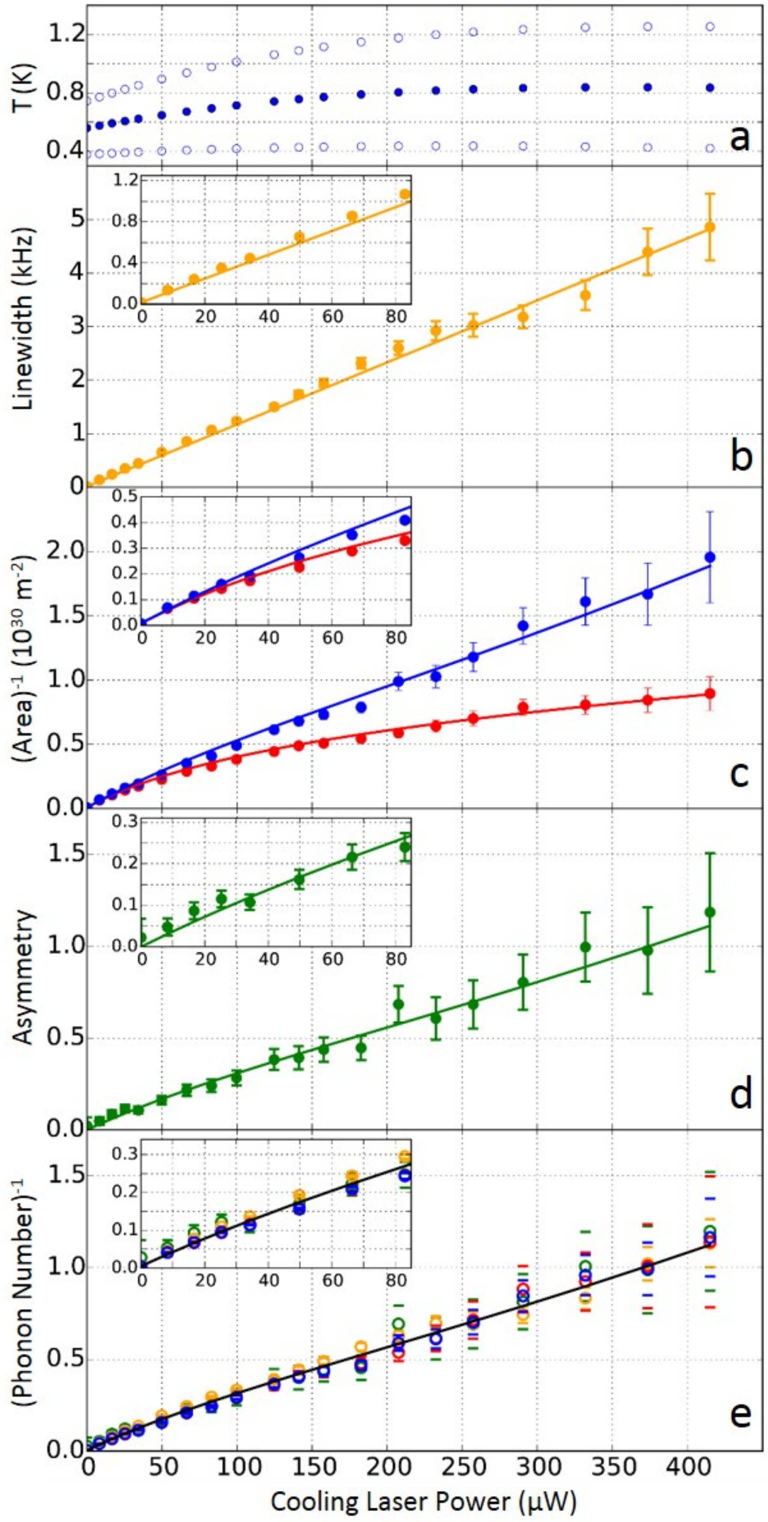
T (K)
1.2
0.8
0.4
a
Linewidth (kHz)
0
1
2
3
4
5
1.2
0.8
0.4
0.0
0
20
40
60
80
b
(Area)$^{-1}$ (10^{30} m^{-2})
0.0
0.5
1.0
1.5
2.0
0.5
0.4
0.3
0.2
0.1
0.0
c
Asymmetry
0.0
0.5
1.0
1.5
0.3
0.2
0.1
0.0
d
(Phonon Number)$^{-1}$
0.0
0.5
1.0
1.5
0.3
0.2
0.1
0.0
e
0
50
100
150
200
250
300
350
400
Cooling Laser Power (μW)

References

---

[1] M. Aspelmeyer, T. J. Kippenberg, and F. Marquardt, Rev. Mod. Phys. **86**, 1391 (2014).

[2] Yiqui Ma et al., Phys. Rev. Lett. **113** 151102 (2014).

[3] A. H. Safavi-Naeini and O. Painter, New J. Phys. **13**, 013017 (2011).

[4] C. A. Regal and K. W. Lehnert, J. Phys. **264**, 012025 (2012).

[5] O. Romero-Isart, Phys. Rev. A **84**, 052121 (2011).

[6] Huan Yang et al., Phys. Rev. Lett. **110**, 170401 (2013).

[7] Stefan Nimmricther, Klaus Hornberger, and Klemens Hammerer, Phys. Rev. Lett. **113**, 020405 (2014).

[8] K. Hammerer et al., Phys. Rev. Lett. **103**, 063005 (2009).

[9] K. Hammerer et al., Phys. Rev. Lett. **102**, 020501 (2009).

[10] K. Stannigel et al., Phys. Rev. Lett. **105**, 220501 (2010).

[11] P. Rabl et al., Nature Physics **6**, 602 (2010).

[12] A. D. O'Connell et al., Nature **464**, 697 (2010).

[13] F. Lecocq et al., Nature Phys. **11**, 635 (2015).

[14] Stephen D. Bartlett et al., Phys. Rev. Lett. **88**, 097904 (2002).

[15] Farid Ya. Khalili et al., Phys. Rev. A **86**, 033840 (2012).

[16] A. J. Weinstein et al., Phys. Rev. X **4**, 0410013 (2014).

[17] Amir H. Safavi-Naeini et al., Phys. Rev. Lett. **108**, 033602 (2012).

[18] N. Brahms et al., Phys. Rev. Lett. **108**, 133601 (2012).

[19] E. E. Wollman et al., Science **349**, 952 (2015).

[20] J. C. Sankey et al., Nature Phys. **6**, 707 (2010).

[21] A. A. Clerk, Phys. Rev. A **84**, 043824 (2011).

[22] T. P. Purdy, R. W. Peterson, and C. A. Regal, Science **339**, 801 (2013).

[23] T. P. Purdy et al., Phys. Rev. X **3**, 031012 (2013).

[24] R. W. Andrews et al., Nature Phys. **10**, 321 (2014).

[25] D. Lee et al., Nat. Comm. **6**, 6232 (2015).

[26] A. Jöckel et al., Nature Nanotech. **10**, 55 (2015).

[27] Andreas Sawadsky et al., Phys. Rev. Lett. **114**, 043601 (2015).

[28] Mingyun Yuan et al., ArXiv:1507.08898 (2015).

[29] J. D. Thompson et al., Nature **452**, 72 (2008).

[30] B. M. Zwickl et al., Appl. Phys. Lett. **92**, 103125 (2008).

[31] A. M. Jayich et al., New J. Phys. **14**, 115018 (2012).

---

[32] I. Wilson-Rae et al., Phys. Rev. Lett. **99**, 093901 (2007).

[33] F. Marquardt et al., Phys. Rev. Lett. **99**, 093902 (2007).

[34] T. P. Purdy et al., Phys. Rev. A **92**, 031802(R) (2015).